Geophys. J. Int. (2009) **179,** 1169–1185 doi: 10.1111/j.1365-246X.2009.04338.x

Inferring the thermochemical structure of the upper mantle from seismic data

Fabio Cammarano,[1] Barbara Romanowicz,[2] Lars Stixrude,[3] Carolina Lithgow-Bertelloni[3] and Wenbo Xu[4]

[1] *Geophysical Fluid Dynamics, ETH Zürich, Sonneggstrasse* 5, 8091, *Switzerland. E-mail: fabio.cammarano@erdw.ethz.ch*
[2] *Berkeley Seismological Laboratory, University of California,* 215 *McCone Hall, Berkeley,* CA 94720, *USA*
[3] *Department of Earth Sciences, University College London, Gower Street,* WC1E 6BT, *UK*
[4] *Department of Geological Sciences, University of Michigan, Ann Arbor,* MI 48104, *USA*

Accepted 2009 July 14. Received 2009 July 8; in original form 2009 April 24

SUMMARY

We test a mineral physics model of the upper mantle against seismic observations. The model is based on current knowledge of material properties at high temperatures and pressures. In particular, elastic properties are computed with a recent self-consistent thermodynamic model, based on a six oxides (NCFMAS) system. We focus on average structure between 250 and 800 km. We invert normal modes eigenfrequencies and traveltimes to obtain best-fitting average thermal structures for various compositional profiles. The thermochemical structures are then used to predict long-period waveforms, *SS* precursors waveforms and radial profiles of attenuation. These examples show the potential of our procedure to refine the interpretation combining different data sets.

We found that a mixture of MORB and Harzburgite, with the MORB component increasing with depth, is able to reproduce well all the seismic data for realistic thermal structures. If the proportions of MORB with depth do not change, unrealistic negative thermal gradients below 250 km would be necessary to explain the data. Equilibrium assemblages, such as pyrolite, cannot fit the seismic data.

The elastic velocities predicted by the reference mineral physics model tested are too low at the top of the lower mantle, even for the fastest (and most depleted) composition, that is, harzburgite. An increase in V_P of 1 per cent and in V_S of 2 per cent improves the data fit significantly and is required to find models that fit both traveltimes and normal modes, indicating the need for further experimental measurements of these properties at the simultaneously elevated pressure–temperature conditions of the lower mantle.

Extending our procedure to other seismic and density data and interpreting the 3-D structure holds promise to further improve our knowledge of the thermochemical structure of the upper mantle. In addition, the same database of material properties can be used in dynamic models to test whether the thermochemical structure inferred from geophysical observations is consistent with the Earth's evolution.

Key words: Composition of the mantle; Elasticity and anelasticity; Body waves; Surface waves and free oscillations.

1 INTRODUCTION

The knowledge of the thermal (T) and compositional (C) state of a large part of the upper mantle relies mostly on the interpretation of seismic data based on knowledge of the elastic and anelastic properties of mantle minerals. Uncertainties in mineral physics and seismic data hamper precise estimations and, in principle, both should be considered simultaneously to properly assess their effects.

Previous work showed that even considering all the uncertainties in the elastic and anelastic properties of mantle minerals, it is very difficult to fit seismic traveltimes and fundamental modes with the simplest thermochemical average mantle structure, that is, a 1300 °C adiabat plus pyrolite composition (Cammarano *et al.* 2005a). The seismic depth profiles of the best-fitting models found in that study, called PREF models, are very similar. This is due to the fortuitous combination of constraints from mineral physics and seismic data. Teleseismic traveltimes and fundamental mode eigenfrequencies used in that work are mostly sensitive, respectively, to the integrated average velocities throughout the upper mantle and to the seismic structure of the shallow upper mantle (100–200 km). In

addition, for a given thermal and compositional structure, mineral physics data provide good constraints on the velocity gradients with depth.

In a following study (Cammarano & Romanowicz 2007), we inverted the long-period seismic waveform database assembled for mantle tomography at Berkeley (e.g. Panning & Romanowicz 2006) by using one of the PREF models as starting model instead of the more commonly used seismic reference model PREM (Dziewonski & Anderson 1981). These long-period data (periods >60 s) are able to resolve average shear velocities throughout the upper mantle. Except in the proximity of the main mantle discontinuities, we obtained a good characterization of the absolute isotropic V_S of the upper mantle. We found that a higher V_S gradient compared to the starting PREF model was required, globally, between 250 and 350 km. The long-period data also required lower seismic velocities than PREF, and even PREM, in the lower part of the transition zone (TZ) (∼600 km). The most plausible explanation for the seismic features required by the long-period data is that the composition becomes more enriched with depth, that is, with more garnet and pyroxenes and less olivine. Alternatively, an unrealistically strong negative thermal gradient with depth would need to be invoked. The purely thermal explanation is not only unphysical, as discussed in Cammarano & Romanowicz (2007), but it would imply intrinsic values of Q_S (shear quality factor) that are too high compared to the values compatible with global observations of seismic attenuation (see Cammarano & Romanowicz 2008). We also speculated that a purely compositional explanation would be consistent with an upper mantle that is not chemically equilibrated, but contains 3-D compositional heterogeneity at a scale beyond the resolution of the long-period data used in that study. This would also be consistent with independent speculations on compositional heterogeneity based on geochemical arguments (e.g. Anderson 2006). Our results are supported by the convection models of Tackley *et al.* (2005, and references therein). These models of mantle convection include two compositional endmembers, that is, MORB and harzburgite components, with their respective phase transitions. A harzburgite layer just below the 660 km is dynamically formed because of the density crossover of the two systems (already known since Irifune & Ringwood 1993). This feature, although not precluding the penetration of slabs, contributes to alter the chemical composition of the whole mantle. For the upper mantle, a gradual enrichment in the MORB component with depth is predicted, consistent with the interpretation of our seismic observations.

Stixrude & Lithgow-Bertelloni (2005b) found that increasing silica-enrichment with depth could help to explain the large seismic velocity gradient seen in seismological models between 200 and 400 km depth. Cobden *et al.* (2008) found further evidence for such compositional structure of the upper mantle. They investigated different average thermal (T) and compositional (C) structures, taking into account the uncertainties in mineral physics data, including the equation of state, and they checked how well the predicted structures fit traveltime data, independent constraints on average velocities and their gradients with depth and arrival times of *SS* precursors from the main mantle discontinuities. In addition to confirming that adiabatic pyrolite cannot achieve the required velocity gradient between 250 and 350 km, they found that higher velocities than those of adiabatic pyrolite are more likely just below 660 km, which again is consistent with the dynamic C structure produced by recent dynamic models.

Recently, Xu *et al.* (2008) described the concept of a mechanical mixture of MORB and harzburgite versus an equilibrium assemblage. Differentiation through partial melting at mid-ocean ridges produces basalts and leaves behind the depleted component, that is, harzburgite. Mantle convection will tend to stir together the two end-members, through stretching, folding and thinning, but low chemical diffusivities preclude chemical re-equilibration over timescales approaching 1 billion years. At the two extremes, mantle composition can be either fully equilibrated or separated into a mixture of MORB and harzburgite. For the same bulk composition in oxides, the two cases are characterized by significant differences in seismic structure, as clearly shown in Xu *et al.* (2008). For example, in the case of a mixture of MORB and harzburgite, free silica will always be present, because it is stable in MORB composition as quartz at shallow depth, then as coesite and below ∼310 km as stishovite. This is not the case for an equilibrium assemblage.

Compositional heterogeneity has been also invoked to explain *SS* and *PP* precursor data, which are sensitive to impedance jumps at mantle discontinuities (e.g. Shearer 2000; Chambers *et al.* 2005; Schmerr & Garnero 2007). Further evidence of a heterogeneous upper mantle is given by the strong seismic scattering documented in all the available high resolution explosion seismic profiles from Siberia and North America (Thybo *et al.* 2003).

A non-linear procedure that accounts for the uncertainties in mineral physics and seismic data should be preferred when inverting for T and C of the mantle, but this approach has some intrinsic limitations. As shown by Cobden *et al.* (2008), such a procedure is successful for inferring the most likely average thermal and compositional structure of the upper mantle. Because of the several parameters involved, however, this approach becomes computationally very intensive if several types of seismic data are tested together and the analysis of the results is sometimes not straightforward. For example, it is difficult to invert seismic data for mineral physics parameters keeping a rigorous thermodynamic consistency of the outcome. In doing such an inversion in previous studies (e.g. Cammarano *et al.* 2005a,b; Cobden *et al.* 2008), it was necessary, for example, to decouple the phase equilibria from the elastic properties and we could not avoid the testing of combinations of parameters which lead to values that were outside the experimental range. Also, some of the combinations produced unphysical results, for instance negative velocity gradients in the lower mantle (Cammarano *et al.* 2005b). In addition, it is extremely difficult for a fully non linear procedure to assess the role of the mineral physics uncertainties compared to the role of alternative T and C structures in fitting seismic data. An exhaustive test of each set of mineral physics parameters should involve a complete characterization of the T–C structures based on all available geophysical measurements. This becomes practically impossible when including the effects on 3-D variations of geophysical observables is desired.

To work around these problems, we here propose a simpler alternative procedure. We consider a starting mineral physics model as our reference. The model is based on the state-of-the-art knowledge of material properties at high pressure and temperature and predicts values of physical parameters (e.g. V_S, V_P, ρ, Q_S) as a function of pressure (or depth), temperature and composition. This reference model can be tested against any set of seismic (and other) data. First, a non-linear inversion for average T and C is performed to find a family of best-fitting models for the data used. The trade-off between T and C can be reduced based on geodynamic considerations and/or by the combination of seismic data that are sensitive to T and C in a different manner. In general, it is possible to combine different data to test the reference physical model. For example, including observations of seismic attenuation, which are mostly sensitive to

temperature, can help to discriminate between *T* and *C* structures that fit equally well other seismic data (e.g. Dalton *et al.* 2009) or we can analyse if and which *T*–*C* structures are able to fit together global teleseismic *P* and *S* traveltime data. Indeed, a nice property of the proposed methodology is that it is always possible to sequentially add new constraints to refine the interpretation. For instance, even if long-period waveform data are not sensitive to mantle discontinuities, the *T*–*C* structures that are able to fit those data will also reproduce the fine structure of the mantle phase transitions as predicted by the mineral physics model. Subsequently, it is possible to test these structures with data that are sensitive to discontinuities, such as *SS* precursors. A careful analysis of the data and their combination will also help to identify problems with the mineral physics model, as we will see in what follows. Once the average structures have been found, it is possible to use them as starting models for 3-D inversion. Also in this case, it will be possible to couple different observations within the overarching *T*–*C* interpretation.

In this paper, we invert a variety of seismic data for average *T*–*C* structure of the upper mantle. We consider fundamental mode and overtone eigenfrequency measurements, weighting them according to their depth sensitivity. We also include *P* and *S* teleseismic traveltimes in our inversion. The seismic data selected are particularly suitable to constrain the average velocities throughout the upper mantle. We investigate both the case of an equilibrium assemblage and that of a mechanical mixture of MORB and harzburgite for some given compositional structures. Additionally, we predict features that can be checked by using other seismic data, thus providing some examples of validation tests. Specifically, we check how the predicted 1-D structures fit, overall, the Berkeley catalogue of long-period waveforms; we show examples of the predicted *SS* precursors waveforms compared to the traces of seismic reference models and we test predicted *Q* profiles against measurements of seismic attenuation. The few examples of validation tests are by far not exhaustive, but give a flavour of the potential of our procedure. In future work, we will extend our procedure to 3-D models, combining different data sets.

2 THE MINERAL PHYSICS MODEL

The fundamental ingredients for determining the elastic properties of multiphase assemblages (rocks) as a function of pressure, temperature and composition are the phase equilibria, that is, the stable mineral phases, their proportions, and compositions, the elastic properties of each phase and an averaging scheme for the whole assemblage. The problem is solved by applying a recently developed thermodynamic theory which, unlike other approaches, permits self-consistent computation of phase equilibria and all elastic properties (Stixrude & Lithgow-Bertelloni 2005a). The stable phase assemblage is determined with Gibbs free energy minimization. Elastic properties for each phase are computed self-consistently, via strain derivatives of the Gibbs free energy, and the average properties of the multiphase assemblage are obtained via the Voigt–Reuss–Hill averaging scheme (Hill 1952). The parameters which define the material properties and phase equilibria are given for the six-component system (Na_2O–CaO–FeO–MgO–Al_2O_3–SiO_2, or NCFMAS) by Xu *et al.* (2008). The addition of sodium produces velocities and phase equilibria that differ substantially from the more limited CFMAS system studied by Cobden *et al.* (2008) for basalt-rich compositions. The model covers the entire pressure and temperature range of Earth's mantle and compositions ranging from harzburgite to basalt. Conversion from pressure to depth is performed using the PREM pressure profile (Dziewonski & Anderson 1981). We will refer to the theory and parameter set together as the XSLB08 model.

Uncertainties in all parameters are reported in Xu *et al.* (2008), including those resulting from experimental uncertainties in the location and Clapeyron slopes of phase transformations, and in the elastic properties of individual phases. Analysis of these uncertainties reveals that the pressure dependence of elastic properties are better resolved than the temperature dependence, and that the bulk modulus is resolved better than the shear modulus. Despite important recent progress (Irifune *et al.* 2008) there is still a need for experimental data at conditions of simultaneously elevated mantle pressure and temperature conditions, particularly at lower-mantle conditions. The seismic data used in this study are very sensitive to the velocity at the top of the lower mantle, and are more sensitive to the absolute pressure of phase transformations, rather than their Clapeyron slopes. Because much of the mantle pressure–temperature regime lies outside the realm of direct experimental constraints, the theory upon which extrapolations are based is an important consideration. In developing the theory (Stixrude & Lithgow-Bertelloni 2005a,b) Stixrude & Lithgow-Bertelloni (2005a) considered many alternative functional forms, choosing a form that is thermodynamically self-consistent, and which is most consistent with existing results from experiment and first principles theory. Cobden *et al.* (2008) investigated the effects of various functional forms on extrapolated properties.

Anelastic properties are much more uncertain than elastic properties. Uncertainty still exists as to the dominant attenuation mechanisms at seismic frequencies, and no experimental data yet exists at elevated pressure. For this reason, we approximate anelastic properties with simple physical laws that are valid for the bulk assemblage. We model the *P*, *T* and frequency dependency of anelasticity by using the model Q5 of Cammarano *et al.* (2003). It is based on the Arrhenius law as expected of thermally activated processes. The model is a hybrid, which accounts for the experimentally observed Arrhenian temperature dependence of the viscoelastic relaxation mechanisms responsible for seismic attenuation, and uses constraints from seismically observed attenuation to adjust the pre-exponential value of the law. The *P* dependence is modelled with a homologous *T* approach (Karato 1993): the attenuation is scaled at any depth with respect to the solidus temperature. Although the solidus varies with composition, we prefer to not model *Q* variations due to composition. We use therefore the pragmatic approach of scaling *Q* only with the solidus curve for fertile peridotite (KLB1, Hirschmann 2000). In other words, we only consider the *T* dependence of *Q* and we assume the *C* dependence to be 0. Based on current knowledge, this assumption is justified. Indeed, other assumptions have the potential to introduce large errors. For example, adopting an attenuation law for the whole rock is probably not appropriate if the compositional state of the upper mantle is as heterogeneous as it seems. The frequency dependence is fixed at 0.2, in agreement with experiments and seismic observations (e.g. Romanowicz & Mitchell 2007). We also tested alternative physical models of *Q*, including the fully experimentally based Faul & Jackson (2005) law, in which the attenuation also depends on grain size. It is worth pointing out that the seismic data used in this paper are not very sensitive to variations in attenuation, although we show that discrimination is possible with observations of seismic attenuation. Considering the fragile state of experimentally based *Q* models, we also present results using a seismic attenuation model: QL6 (Durek & Ekström 1996). This model has been built with attenuation data of long-period waves (periods between 150 and 300 s) and is

therefore appropriate for the modelling of normal mode data that are sensitive to the upper mantle.

A short review of uncertainties in anelastic properties can be found in Cammarano & Romanowicz (2008). A more extended review, also illustrating the principles of the physical mechanisms responsible for attenuation, is given by Jackson (2008). Experiments confirm the strong temperature dependence and give insight into the possible mechanisms governing the intrinsic seismic attenuation. Grain size dependence of attenuation has been also found and modelled by Faul & Jackson (2005). A small amount of water appears to enhance attenuation significantly, although the relationship is not fully quantified (Aizawa *et al.* 2008). Effects of dislocations, which can have a role for the upper mantle, have not yet been estimated in laboratory experiments. More uncertain is the pressure dependence: the activation volume is unknown, which justifies the adoption of alternative models that assume a constant relation between activation enthalpy and the solidus temperature (T_S). This scaling relation, known as Weertmans law (Weertman 1970), or homologous temperature approach, is expressed as $g = H/RT_S$, where R is the gas constant and the constant g is usually estimated around 30 for the upper mantle (Karato 1993). In the model Q5 used in this study, we assume as well a value of $g = 30$ (Cammarano *et al.* 2003). The measured frequency (ω) dependence is quite low, ranging from 0.1 to 0.3 (Jackson 2008). These values are consistent with the observed frequency dependence in seismic observations (e.g. Romanowicz & Mitchell 2007).

3 PROCEDURE

Once we have a clear definition of our reference mineral physics model, we can search for the thermochemical structures related to this model that are able to fit seismic data. In order to invert for T and C, it is important to decide what kind of variations in composition we want to test. In theory, it is possible to vary each of the six modelled oxides and test all possible combinations. The composition of the upper mantle is evolving through melting extraction, however. It is natural, therefore, to think in terms of basalt depletion. In other words, we expect that the variations in C within the mantle align along a compositional axis that goes from harzburgite to MORB. In this paper, we consider either an equilibrium composition or a mechanical mixture of the two end members.

We show the results for two different compositional profiles (Fig. 1), that are a pyrolite model (C1), a model which reproduces the features of the Tackley's (Tackley *et al.* 2005) geodynamic models (C2). We also tested a model similar to C2, but without the depleted layer at the top of the lower mantle. We will focus on the upper mantle average structure from 250 to 800 km depth. The exact chemical composition of MORB, Harzburgite and pyrolite used in this paper are the same given in Xu *et al.* (2008).

The procedure consists of the following steps for each C structure.

(1) Apply starting seismic constraints in order to reduce the T structures to test.

(2) Compute 1000 T structures and predict their seismic structure by using the reference mineral physics model.

(3) Compute P and S traveltimes and the eigenfrequencies of fundamental modes and first three overtone branches and compare with data.

(4) Determine the best-fitting T–C models for all the data used.

(5) Validate these models with global measurements of seismic attenuation, long-period waveforms and show predictions of SS precursors waveforms.

3.1 Starting seismic constraints

In order to reduce our search to T–C models that are likely to fit the seismic data, we use seismic constraints from previous studies. The best insight on the average seismic structure of the upper mantle comes from the interpretation of long-period data, which are mostly sensitive to shear velocity. In Fig. 2, we show the isotropic V_S for some global models. One feature that produced much confusion for the interpretation of seismic velocities was the large discontinuity in model PREM at 220 km (the so-called Lehmann discontinuity). This feature was imposed as an *a priori* constraint on starting models, in agreement with the conjecture of a main global boundary at this depth. Such a large global discontinuity cannot be explained by common petrological mantle models. Its presence not only requires a physical interpretation, but also affects the velocity gradients of the PREM model in a large depth range. It is now recognized that such a feature is not global and likely includes several discontinuities at different depths that probably do not share the same physical origin. Moreover, changes in radial anisotropic structure can be significant (Gaherty & Jordan 1995; Gung *et al.* 2003). Indeed, the new global model from the Harvard group (Kustowski *et al.* 2008, called

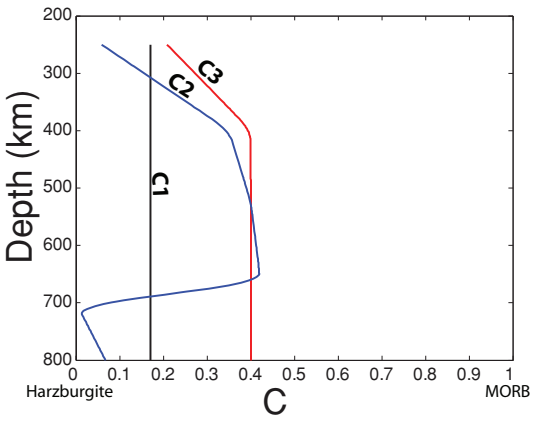

Figure 1. The three compositional profiles tested. Composition is normalized from 0 Harzburgite to 1 MORB.

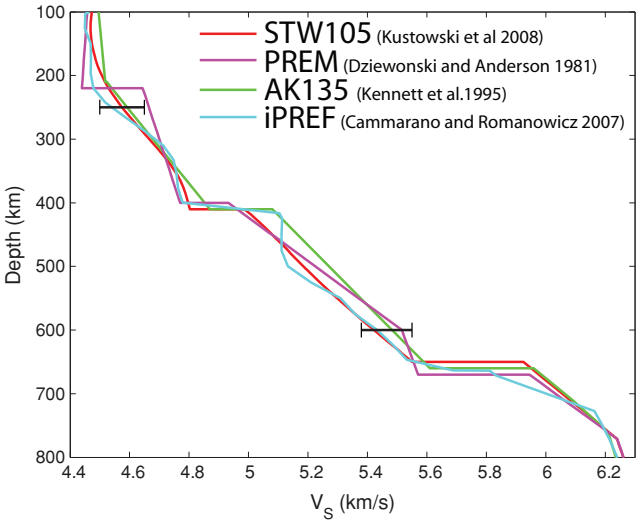

Figure 2. Isotropic V_S upper-mantle models (see legend). Range of velocities expected at 250 and 600 km are in black.

STW105, also in Fig. 2), does not have any sharp discontinuity at 220 km. The iPREF model (Fig. 2) is the global average of the 3-D model of Cammarano & Romanowicz (2007). This model is based on an inversion of long-period waveforms starting from a physical reference (PREF) model. The model AK135 (Kennett *et al.* 1995) is plotted for completeness. This model is obtained by inversion of teleseismic traveltimes and does not have any constraints on upper-mantle structure apart from its integrated value. It must be recalled that the goal of the authors was to construct a better global model for earthquake location and not to study upper-mantle structure. We also recall that the model has continental lithosphere structure in the first 150 km in order to account for the continental bias of traveltime data. The new Harvard reference model, STW105, also differs from PREM by having radial anisotropy that extends down to 400 km, though it decreases significantly with depth. Owing to the absence of the 220 km discontinuity, V_S at 250 km is significantly lower than in PREM and the velocity gradient between 250 and 350 km is much higher. Both values are now closer to the iPREF ones. Note that a direct comparison of the STW105 and iPREF isotropic models is not straightforward, because iPREF is an average of a 3-D model and the anisotropic parts of the models are different. STW105 is characterized by a slower mid transition zone than in PREM. We suspect that the discrepancy between PREM and STW105 does not depend much on the more extended data set used in the latter model, but rather on the different choices made to model the discontinuities. For example, the transition from upper to lower mantle is fixed at 650 km in STW105 instead of at 670 km, as in PREM. Note that the global models do not have a direct constraint on the depth of mantle transitions and rely on independent observations, based on studies of reflected and converted phases at the mantle discontinuities. We note that the V_S of the iPREF model is very similar to STW105 around 600 km. In the iPREF model, the discontinuities come from mineral physics data and have a finite depth interval. For example, the olivine-wadsleyite transition, responsible for the so-called 410 km discontinuity, occurs within a $\sim$12 km interval. Based also on previous tests on the dependence of the outcome from the starting model (see Cammarano & Romanowicz 2007), we are confident that the values of STW105 and iPREF in the mid transition zone are more robust than PREM. All together, these considerations allow us to impose constraints on absolute V_S at 250 and 600 km (Fig. 2) and on the velocity gradient with depth from 250 to 320 km. Specifically, all our models will have $4.5 < V_S(250) < 4.65$, $5.35 < V_S(600) < 5.5$ km s^{-1} and $dV_S/dz(250–320)$ km between 1.7 and 2.8 $\times$ 10^{-3} s^{-1}. The given V_S boundaries are readily transformed into thermal boundaries for any composition by using the reference mineral physics model. The temperature boundaries predicted at 250 and 600 km by the XSLB08 model with Q5 attenuation are given in Fig. 3.

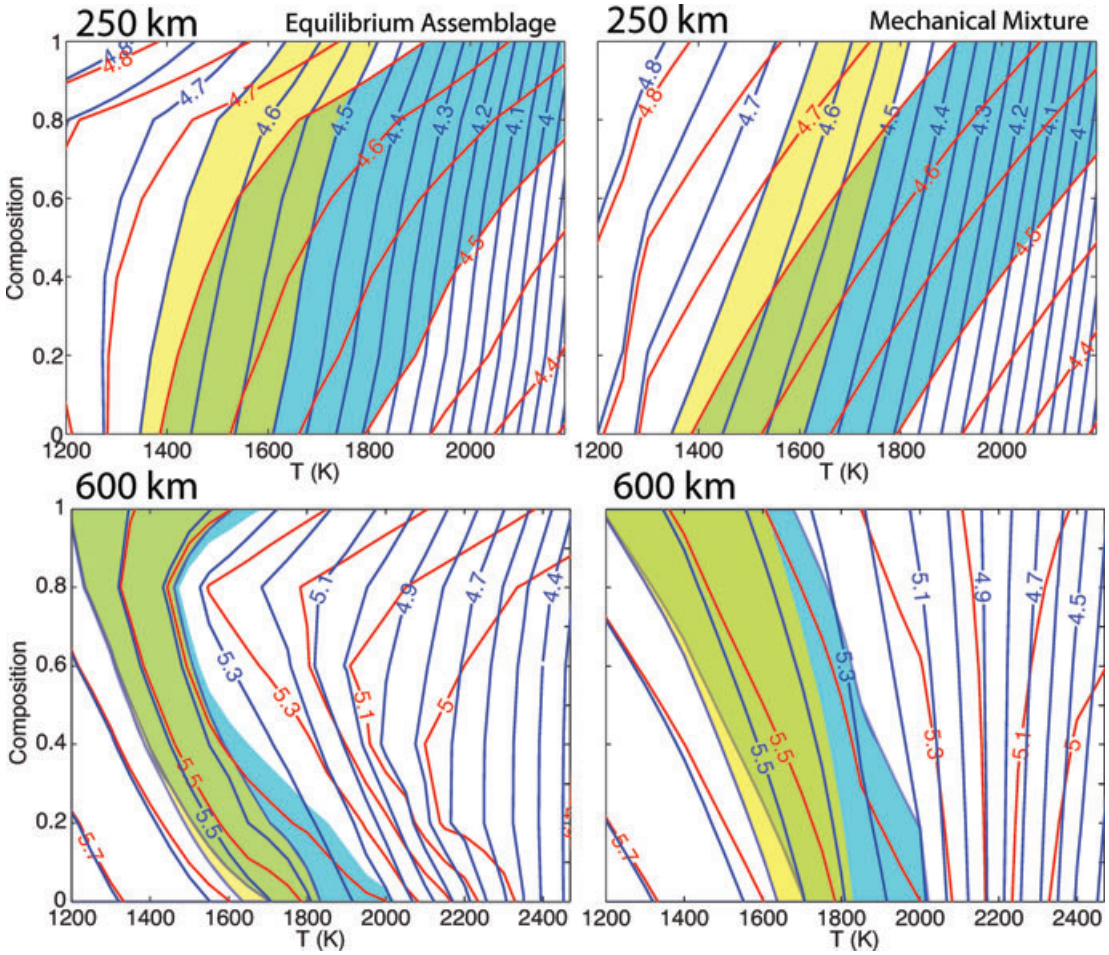

Figure 3. Predicted V_S (blue contours) as function of temperature and composition (0 is Harzburgite, 1 is MORB) with the reference mineral physics model at 250 km (top panels) and 600 km (bottom panels). Right panels are for a mechanical mixture MORB-Harzburgite, left panels for an equilibrium assemblage. Purely elastic velocities inferred from XSLB08 are in red. Anelasticity corrections are performed with the model Q5. LIght-blue and yellow areas correspond to the thermal boundaries before and after anelasticity correction based on V_S constraints from seismic models.

Purely elastic effects are shown in red contours. Consistently with the P and T dependence of anelasticity, Q effects are more important at shallow depths (top panels) and high T. We note also that the temperature sensitivity increases and becomes dominant over composition when anelasticity effects are modelled (i.e. contour lines get closer and more vertical). The difference between the two shaded areas in Fig. 3 gives an estimate of the Q effects on thermal interpretation of V_S. We verified that Q models other than Q5 have a similar effect. This is true also when we use the seismic model QL6 instead of modelling the P, T and ω dependency based on mineral physics. In a later section, we will again discuss attenuation, as our results can help to get an insight on uncertain parameters that enter into its modelling.

The two boundaries of the V_S gradient with depth between 250 and 320 km are converted into thermal gradient boundaries as a function of the starting T and C at 250 km. Practically, we found the relation between velocity gradient and thermal gradient for a reference C (pyrolite) and T (1700 K) at 250 km and we estimated correction terms when varying the thermal and compositional values at 250 km.

The high velocity gradient required by seismic data below 250 km inform us on the expected T and C structure, as we already discussed in the introduction. Based on the mineral physics model used here, an equilibrium assemblage is not able to explain the seismic observations (Fig. 4). A mechanical mixture has better chances to explain the $\mathrm{d}V_S/\mathrm{d}z$ gradient although a C gradient with depth is still required for any realistic T structure (Fig. 4). For example, fitting the STW105 V_S gradient with a mechanical mixture requires doubling the MORB component in a depth interval of only 70 km, if the thermal structure is a 1700 K isotherm and C at 250 km is pyrolite (Fig. 4). If we assume a more depleted composition at 250 km, we need an even larger compositional gradient with depth. For instance, if C at 250 km is harzburgite, a $\mathrm{d}C/\mathrm{d}z$ of more than 0.25 is required (see top panel in Fig. S1). On the contrary, variations of the reference T at 250 km can help to reduce the C gradient. We computed that an increase of 150 K will reduce the C gradient to 0.1 for an isotherm (at 1850 K, in this case) and a decrease of 150 K will also reduce the C gradient to a value of 0.07 for a 1550 K isotherm (see bottom panel in Fig. S1). The non-linear dependence of the velocity gradients with the starting T at 250 km is due to a combination of thermal effects which modify the phase-equilibria, and elastic and anelastic properties. We do not enter in interpretative details at this point, but we note that for any realistic thermal structure a mechanical mixture plus a compositional gradient with depth are required. Therefore, we will show only the tests regarding the mechanical mixture case in the following steps of the procedure.

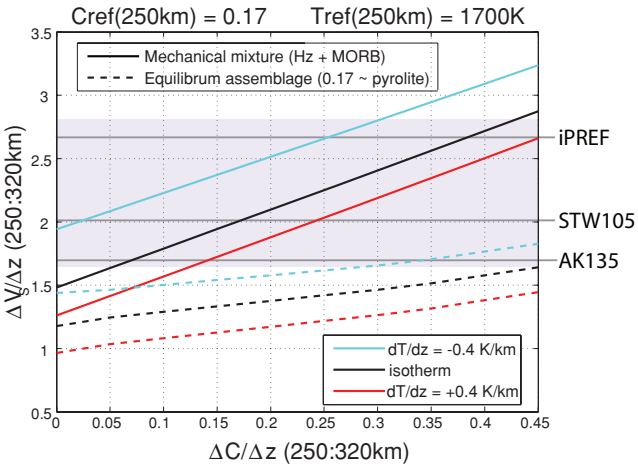

Figure 4. Velocity gradients between 250 and 320 km inferred from our reference mineral physics model (XSLB08+Q5) for different thermal structures (see legend) and as a function of compositional gradient with depth. Solid lines are for mechanical mixture, dashed for equilibrium assemblage. Values of seismic models are plotted as reference. Light grey area is the total range compatible with previous seismic studies. A similar figure, but starting with different C_{REF} and T_{REF} at 250 km is in supporting material, Fig. S2.

The reason why a mechanical mixture is able to obtain a larger V_S gradient than an equilibrium assemblage in this depth range is due to the coesite–stishovite transition which occurs around 300 km (Xu *et al.* 2008). Owing to the relatively small uncertainties in the P derivatives of mantle minerals, this result does not change significantly when other mineral physics models are used (see Cammarano & Romanowicz 2007). This transition has been already proposed in previous studies as the cause for the so-called X-discontinuity around 300 km (e.g. Williams & Revenaugh 2005) and it was also noted as a means of increasing velocity gradients by Cobden *et al.* (2008).

An increase in grain size from order of mm's in the shallow upper mantle to several cm in the transition zone can also help to explain the V_S gradient observed in seismic models (Faul & Jackson 2005). We will ignore the grain size dependence for the moment, but we will discuss its role in a later stage of our procedure.

3.2 Thermal structures

The thermal structures tested have only four parameters. In addition to the three constraints on temperature based on seismic observations, that is, temperatures at 250 and 600 km and $\mathrm{d}T/\mathrm{d}z$ between 250 and 320 km, we also set the thermal gradient below 600 km to be between -0.1 and 0.8 K km^{-1}. For each compositional profile tested, we compute 1000 thermal profiles (all represented in Fig. 8) by varying randomly each of the four parameters within the given boundaries. We smooth the profiles using a common moving average filter. The T structures are defined between 250 and 800 km. We predict V_P, V_S, density, Q_S for all the T–C structures using the reference mineral physics model. The seismic structure in the first 120 km is taken from a seismic reference model. We use AK135 for traveltimes, which, as already mentioned, has a continental lithosphere to account for the data coverage, and STW105 for modes. Possible trade-off effects with shallow structure have been tested by replacing the reference models with others. Below 1000 km, we also use the same seismic reference models. Between 120 and 250 km and between 800 and 1000 km, we merge the values with a simple linear interpolation.

3.3 Fit to seismic data

3.3.1 Normal modes

We compute the eigenfrequencies and eigenfunctions of each model by using a modified version of the code MINOS (by John Woodhouse, see, for a review Woodhouse 1988), named simply 'normal modes'. The code has been developed by Yann Capdeville and it is freely distributed through the SPICE webpage (www.spice-rtn.org/library/software/). The synthetic eigenfrequencies are compared with observations. We use the mode frequency data (${}_n\omega_\ell$) collected and distributed by the Reference Earth Model (REM) webpage: mahi.ucsd.edu/Gabi/rem.dir/surface/rem.surf.html. Specifically, we

use the mean frequencies of the fundamental modes and first three overtone branches ($n = 0$, 1, 2 and 3) of both spheroidal (S) and toroidal (T) components. We use an L1 weighted misfit function for each ${}_nS$ and ${}_nT$, defined as

$$\frac{\sum_{\ell=\ell_{\min}}^{\ell_{\max}} |\Delta\omega_\ell| W_\ell}{\sum_{\ell=\ell_{\min}}^{\ell=\ell_{\max}} W_\ell}, \tag{1}$$

where ℓ is the angular order. $|\Delta\omega_\ell|$ is the residual frequency for each mode between observed and synthetic value, namely

$$|\Delta\omega_\ell| = \left| \frac{{}_{\rm obs}\omega_\ell - {}_{syn}\omega_\ell}{{}_{\rm obs}\omega_\ell} \right|, \tag{2}$$

hence $|\Delta\omega_\ell| = 1$ means that the frequency computed is 100 per cent different from the one observed.

W_l is a weighting factor which is computed according to the depth sensitivity of each mode ${}_nS_\ell$ and ${}_nT_\ell$ in a given depth-range of interest. In general, the modal frequencies are affected by variations in V_P, V_S and ρ as a function of depth. The sensitivity (or Fréchet) kernels for those parameters can be computed for small perturbations for any given spherically symmetric model (Woodhouse 1988; Dahlen & Tromp 1998). The difference in sensitivity between realistic Earth models is small. Therefore, we use the sensitivity kernels computed with the PREM model for our weighting. Note that most of the data used are mostly sensitive to V_S structure, spheroidal modes are weakly sensitive to V_P and only a few of them have a marginal sensitivity to density. The total weight W_ℓ is given by the sum of three different contributions, one for each parameter, which are scaled according to their relative importance.

The weighting factor of each parameter takes into account the relative sensitivity within the depth range compared to the full sensitivity of the mode. In order to do that, we simply divide the sensitivity area inscribed into the depth range by the full sensitivity area. The weight takes a value of 1 if there is no sensitivity outside the considered depth range. On the contrary, if the sensitivity is null inside the depth range, the weight is 0. We show the computed weights for the spheroidal fundamental modes for three different depth ranges within the upper mantle and for the full depth range of interest for this study, that is, 250–800 km depth (Fig. 5). The trend with angular order is consistent with the mode sensitivity. For example, the spheroidal fundamental modes at very low angular orders (low frequencies) are mostly sensitive to lower-mantle structure and the full upper mantle weight approaches 0 at $\ell < 10$. Most of the sensitivity to structure between 600 and 800 km is confined between $15 < \ell < 60$. With increasing ℓ (or frequency), modes become more sensitive to shallow structure. For example, at ℓ around 150 (Fig. 5), the weight between 250 and 800 km (Fig. 5, black curve) is 0.3, that means that the 30 per cent of the sensitivity area is confined within this depth range and the rest lies in the top part above 250 km. Almost 80 per cent of the total value between 250 and 800 km is due to structure between 250 and 400 km (Fig. 5, red curve), only 20 per cent to structure between 400 and 600 km (Fig. 5, light blue). Changes in structure beneath 600 km do not affect this mode (Fig. 5, blue curve). The weights also illustrate trade-off problems between the different depth ranges. For example, the modes that are most sensitive to the depth range from 600 to 800 km are also significantly affected by shallower structure (Fig. 5). We anticipate that the trade-off with shallow structure reduces the potential benefit of analysing modes for each depth range.

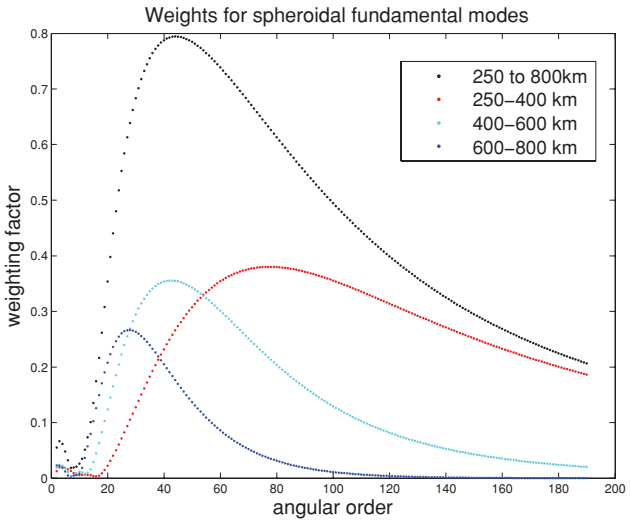

Figure 5. Weights of spheroidal fundamental modes used in this study.

Contributions from V_P and density for the 250-to-800 km depth range are shown in Fig. 6. The ${}_0S$ modes shown here are essentially not sensitive to density, while sensitivity to V_P structure is present. Note that V_P, V_S and ρ are scaled independently in Fig. 6. A given mode has a different sensitivity to changes in V_P and V_S structure for a given depth range. For example, ${}_0S_{20}$ does not have much sensitivity to V_S upper-mantle structure, but it has sensitivity to V_P upper-mantle structure (Fig. 6). This is an expected feature, which is consistent with the shape of the V_P sensitivity kernels compared to the V_S ones, as for example illustrated in the Rogues's gallery of Fréchet kernels in Dahlen & Tromp (1998, p. 345). It is interesting to note, however, that the trade-off between V_S and V_P structure, which is usually tackled by using scaling factors, is an advantage for our investigation of T and C structures of the upper mantle. When varying T and C, we are able to predict the whole seismic structure from our material properties database. In other words, V_P and V_S (and also density) are coupled and we do not need to use any arbitrary scaling factor.

Each normal mode has its own absolute value of sensitivity. For example, fundamental mode kernels are about three times as large

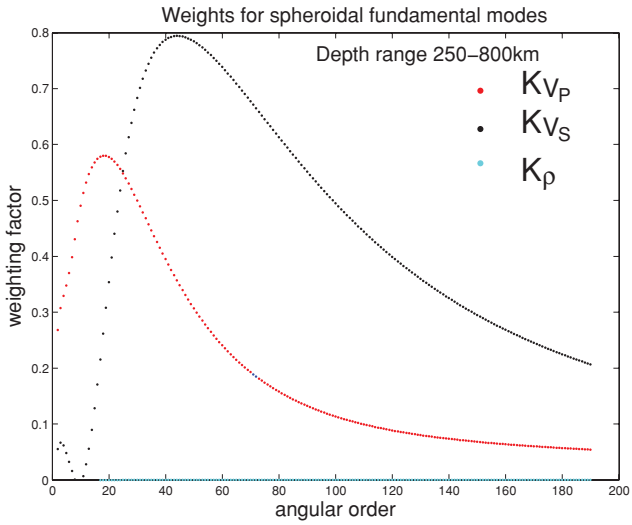

Figure 6. Comparison of individual weights of spheroidal fundamental modes based on V_P, V_S and density sensitivity kernels. Curves are not scaled here to absolute sensitivity to enhance visibility of V_P factors.

as the overtone kernels. We scale each mode branch independently. This way, we are giving a larger weight to the modes that are sensitive to the transition zone structure compared to the fundamental modes at high ℓ (i.e. surface waves).

3.3.2 Traveltimes

P and *S* traveltimes as a function of epicentral distance are computed with the code TauP, developed by Philip Crotwell (Crotwell *et al.* 1999) and also available online (www.seis.sc.edu/TauP/). The code is based on the well-known $\tau - p$ approach of Buland & Chapman (1983). The synthetic traveltimes are compared with the arrivals collected by the International Seismological Center (ISC) since 1964 and reprocessed by Engdahl (Engdahl *et al.* 1998). The catalogue, called EHB, collects more than 10^6 *P* arrivals and 10^5 *S* arrivals. We gather the data in bins of half degree of epicentral distance and we compute the mean values and standard deviations of each bin (same procedure as in Cammarano *et al.* 2005a,b). In this paper, we focus on arrivals beyond 20°. Teleseismic traveltimes are informative on the average V_P and V_S structure of the upper mantle.

The fit to traveltime data is computed with a similar L1 misfit function as used for modes, that is,

$$\frac{\sum_{i=\Delta_{\min}}^{\Delta_{\max}} |\Delta t_i|}{N}, \tag{3}$$

where Δt is the residual time with observations for *P* and *S*, that is $({}_{\rm obs}t - {}_{\rm syn}t)/{}_{\rm obs}t$ and N is the total number of steps in epicentral distance.

3.3.3 Results

In Fig. 7, we show the misfits to mode data computed with a mechanical mixture for the compositional case C1 for the full depth range investigated, that is, 250–800 km. The Q structure is not modelled here, but is given by the seismic model QL6 (Durek & Ekström 1996). We tested that using the *P*–*T* dependent model Q5 at a reference period of 150 s has a negligible effect on the interpretation of normal modes. There are some general features of the mode fits that also occur for the other compositional cases. Only few models among the 1000 tested are able to fit the data almost as well as the seismic reference models (Fig. 7). The normal mode data, hence, discriminate between the *T* models tested. Best-fitting models for fundamental modes (light blue in panel a) also fit overtones sufficiently well. Note, however, some second order effects. For example, the best-fitting models for fundamental modes fits ${}_3T$ better than ${}_3S$ (Fig. 7, panel d). In general, the best-fitting models can reasonably satisfy both spheroidal and toroidal fundamental modes. This is due to the imposed radial anisotropy, taken from the seismic reference model. Nevertheless, we observe in all the panels of Fig. 7, a trend that is indicative of a not perfect correlation between the spheroidal and the toroidal component. We recall that all the models have the same radial anisotropy structure as in STW105 only in the top 120 km while below, in contrast to STW105, anisotropy decreases

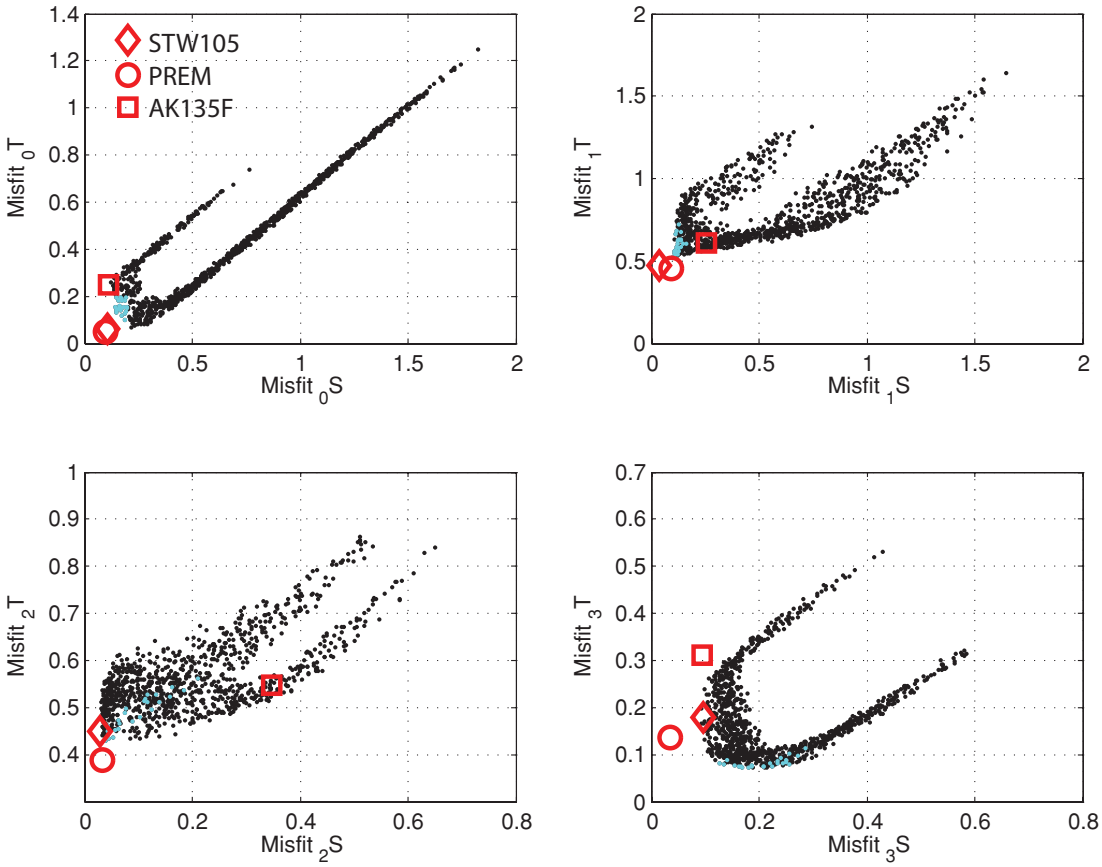

Figure 7. Misfits of normal mode data for 1000 thermal structures and compositional case C1. Panel a for fundamental modes and other panels for overtone branches. In light blue, models which have a misfit <0.2 for both ${}_0S$ and ${}_0T$. Values of seismic reference models are also plotted (see legend).

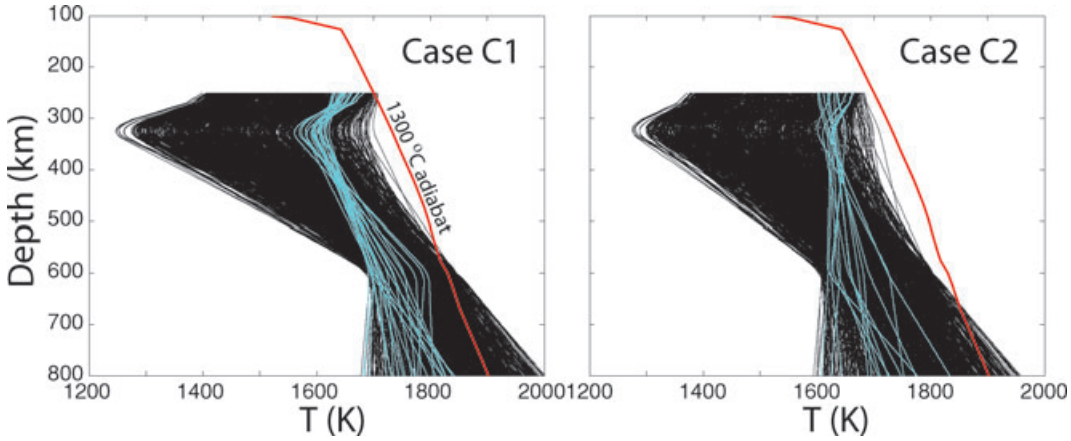

Figure 8. Thermal structures of the 1000 models tested for case C1 (left-hand panel) and C2 (right-hand panel), in black. Thermal structures of the best-fitting models in light blue. The red line is the 1300 °C adiabat. For the compositional case C1, negative thermal gradients are required between 250 and 320 km to fit the seismic data, whereas this is not the case for C2.

linearly down to 250 km, where all the models become isotropic. Therefore, we are probably underestimating the radial anisotropic structure required by the mode data. In theory, it is possible to adjust it in order to improve the fit of the *T*–*C* models tested. This is beyond the scope of this paper, however.

The trade-off between T and C emerges when we compare the thermal profiles of the best-fitting models for the case C1 (pyrolite) and C2 (resembling C profiles obtained from geodynamic modelling) (Fig. 8). A negative thermal gradient just below 250 km is required for C1. This is not the case if there is an enrichment in MORB component (C2). T at 600 km is, in both cases, almost 200 K colder than what is predicted from a $Tp = 1300\,^{\circ}$C mantle adiabat (Fig. 8). Note that the starting seismic constraints already required a relatively cold upper mantle, as illustrated by the full range of thermal structures tested that are compatible with those constraints (Fig. 8). In agreement with the general sensitivity of mode data, the thermal structures of the best-fitting models tend to diverge going deeper.

In Figs 9 (spheroidal modes) and 10 (toroidal modes), we plot the residual frequencies for all the best-fitting models for the case C1. The respective figures for the case C2 are given in Figs S2 and S3. A common feature of all the compositional cases tested is that it is not possible to fit certain specific modes. Specifically, the observed frequencies are systematically larger than the modelled ones at ℓ between 10 and 30 for both spheroidal and toroidal fundamental modes; at $\ell > 30$ for ${}_1S$, at ℓ between 20 and 40 for ${}_1T$ and at $\ell >$ 35 for ${}_2T$. (Figs 9 and 10) All the modes that we are not able to fit are particularly sensitive to the deeper part of the investigated structure. According to the positive sensitivity kernels, velocities at the top of the lower mantle should increase in order to increase the frequencies in our synthetic models. Note also that fundamental spheroidal modes at high angular orders have a systematic bias as well. This depends on the shallow structure which is given by STW105 and is not a problem for our study.

The best-fitting models for normal mode data do not fit traveltimes. Their residuals to *P* and *S* arrival times are in Fig. 11 (green models, same figure for case C2 is in Fig. S4). These models have a negative baseline shift of ∼2 s for *P* and of ∼6 s for *S*. The best-fitting models for traveltimes, for which we also plot the residuals in Fig. 11 (black models), are characterized by higher average velocities of the upper mantle. In terms of temperature, this translates into a colder upper mantle compared to what is required by mode data. Note that for traveltimes calculations we use a continental shallow structure, taken from the AK135 model. The baseline shift of the teleseismic traveltimes will get even worse if we use an average model. More importantly, all the models tested have a sharp decrease in the residual shape at far-regional distance (epicentral distances <30°, Fig. 11). The turning point of the rays at epicentral distance of 20° is around the bottom of the upper mantle for both *P* and *S*, while at 30° the rays turn at a depth around 770 km. The best-fitting traveltime models are characterized by a strong positive residuals at 20°, that is fully recovered at 30° (Fig. 11). This means that the upper mantle is, on average, too fast (and cold) according to the data and the portion of the mantle right below the 660 is too slow. In other words, the best-fitting models for traveltimes balance the too low velocities which characterize all the models at the top of the lower mantle (and for any compositional case) with a faster upper mantle. Note again that teleseismic traveltimes are only sensitive to the integrated upper-mantle structure.

The upper-mantle seismic structure of the models which fit traveltimes is not only inconsistent with mode data, but also predicts a transition zone thickness of ∼280 km that is too large compared to what is inferred from independent studies on reflected and converted seismic phases at the mantle transitions around 410 and 660 km. On the other hand, the seismic structure of the models that fit normal modes is consistent with the observed average thickness of the transition zone (Fig. 12, models for C2 case are in Fig. S5).

Both for the case C1 and C2, the models which fit normal mode eigenfrequencies are characterized by the highest possible velocities at the top of the lower mantle (Figs 12 and 5S). Between the three compositional cases tested, the one with a depleted layer (i.e. harzburgite) right below 660 km (i.e. C2) is able to get the highest velocities at this depth. From the previous analysis, it is clear that the seismic data require, overall, a faster seismic structure at the top of the lower mantle than what is predicted by the mineral physics model. An increase in V_P of 1 per cent and of V_S of 2 per cent at the top of the lower mantle is able to eliminate the discrepancy between the traveltime and normal mode analysis. Additionally, it improves significantly the fit of both modes and traveltimes, eliminating the systematic effects discussed above (see Fig. 13). Using the same selection criteria for the best-fitting models, the number of best-fitting models for either modes or traveltimes increase significantly and now we are able to find models which fit both data sets. For

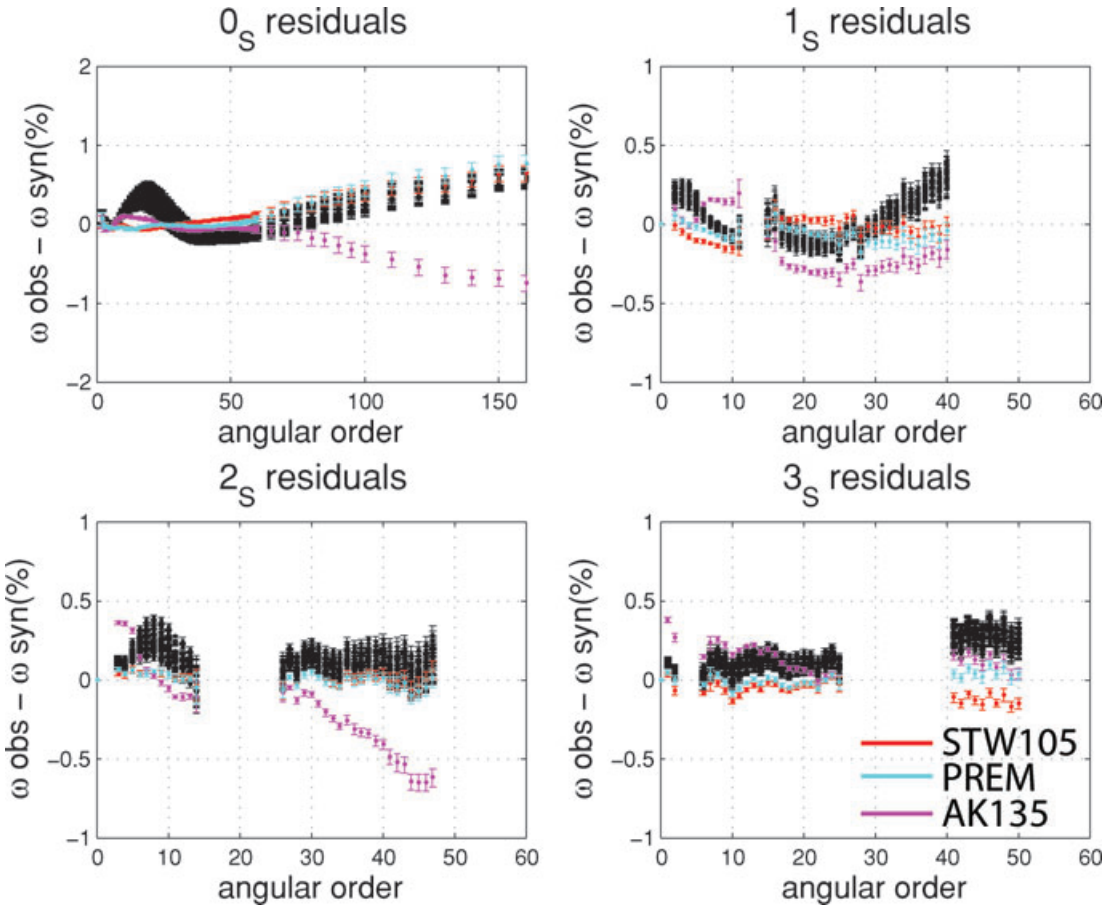

Figure 9. Residual eigenfrequencies for spheroidal modes of the best-fitting models for case C1 (in black, same figure for case C2 is in Fig. S2). The trend of seismic models is also plotted (see legend). Mean frequencies data are from REM webpage. Bounds of residual values refer to the standard deviations of frequency data.

example, if we select for the case C2 only the models which attain a misfit values below 0.2 for ${}_0S$ and ${}_0T$, we count only 14 models out of 1000 before the correction and 52 models after it. For traveltimes, only 20 models have a misfit <0.08 for P and S traveltimes before the correction, while we have 194 models after the increase in velocities. Variations on the same order of magnitude are obtained for the other compositional cases.

In Fig. 13, we present the best-fitting model for modes before (blue) and after (black) the increase in velocities at the top of the lower mantle. The systematic problems at specific angular orders, previously discussed, are gone (top and middle panels). At the same time, the model also fits the traveltimes very well (bottom panels). Note that all the models which fit modes well fit traveltimes as well. A baseline shift of $\sim$1 s for P and $\sim$2 s for S remains. This is probably due to shallow structure. A slightly faster lithospheric part of the model could help to reduce such a baseline shift. We recall we use the continental lithosphere taken from AK135 model, which is already faster than an average model. A more detailed discussion on fitting of the shape and the baseline shift of P and S arrival times can be found in Cammarano *et al.* (2005a).

Within the entire compositional range we have explored, the only way to justify such an increase in velocity at the top of the lower mantle with our reference mineral physics model is to assume a negative thermal gradient between the upper and lower mantle. Assuming we have a depleted layer at the top of the lower mantle, we computed a ΔT of $\sim$140 K. The uncertainties in the mineral physics model are sufficiently large to permit the increase in velocity required by the seismic data, pointing to the need for tighter experimental constraints. Alternatively, a completely different lower-mantle composition, for example, chondritic (Matas *et al.* 2007; Cobden *et al.* 2009), may be required in order to fit the seismic data.

4 VALIDATION TESTS

The previous analysis based on normal modes and traveltimes enabled us to obtain a number of best-fitting thermal models for different C structures. At the same time, the seismic data provide a robust test of the material properties inferred from the mineral physics model. We found that the elastic properties of lower-mantle minerals should be higher than what is modelled in XSLB08. Together with our interpretation in terms of temperature and composition, we also obtain average seismic models (Fig. 12), which not only have a structure consistent with the data inverted, but also predict seismic structure beyond the resolution of the data used.

In what follows, we discuss the consequences that such features have on other data and show some examples of validation tests. We recall that our procedure is twofold: improve knowledge of T and C of the upper mantle and highlight possible problems with the mineral physics parameters used.

In Fig. 14, we compare the seismic and density structure of the best-fitting model with a constant compositional profile (case C1)

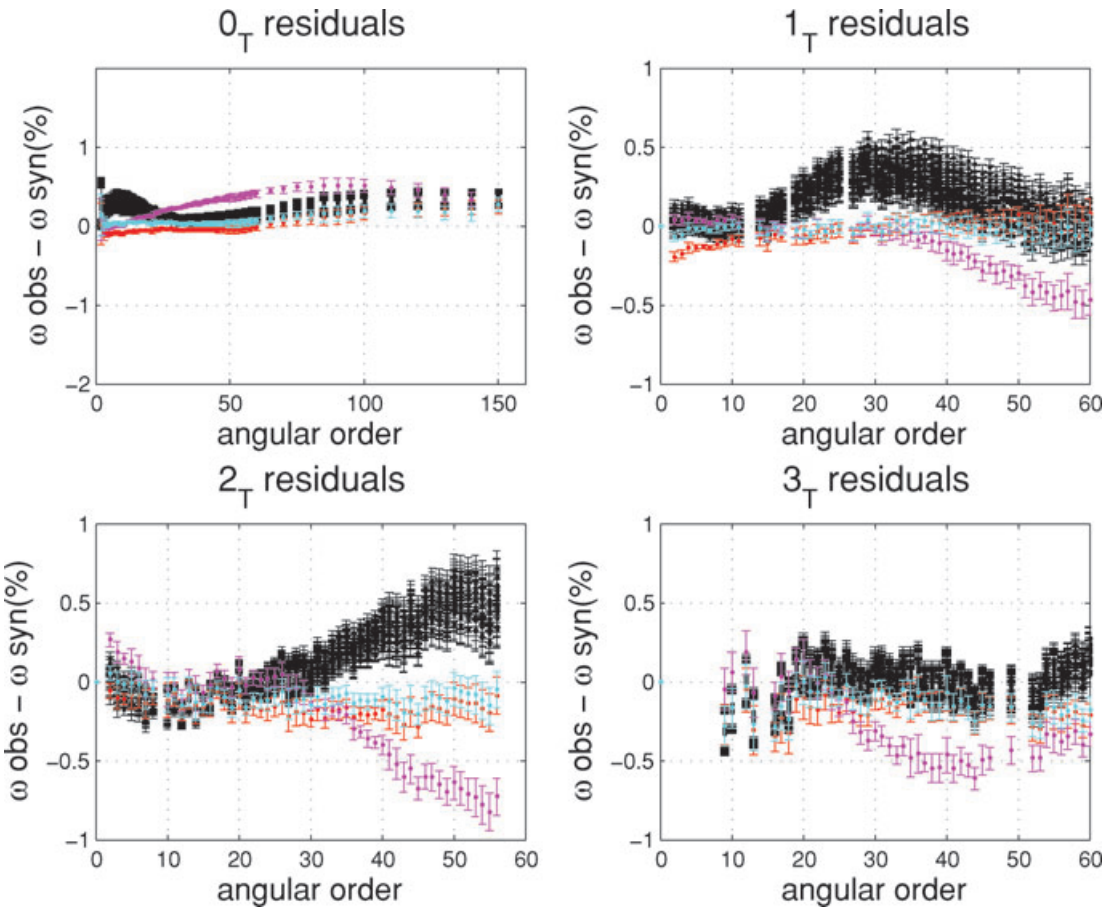

Figure 10. Residual eigenfrequencies for toroidal modes of the best-fitting models, case C1 (same figure for case C2 is in Fig. S3). Seismic models use the same colour scheme of Fig. 9. Mean frequencies data are from REM webpage. Bounds of residual values refer to the standard deviations of frequency data.

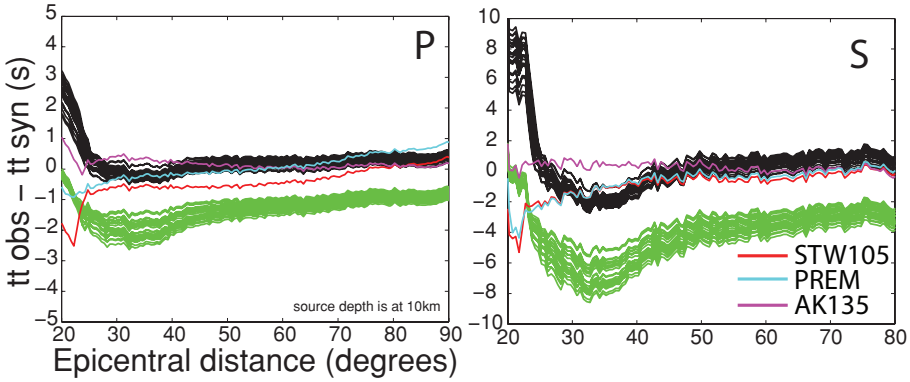

Figure 11. Traveltime residuals for *P* and *S* phases to the EHB data (Engdahl *et al.* 1998) for case C1 (same figure for case C2 is in Fig. S4). In black, best-fitting models for traveltimes, in green best-fitting models for modes. Other lines refer to seismic reference models, see legend.

and that for the more complex compositional profile obtained from modelling results (case C2). The models here presented include the increase in V_P and V_S at the top of the lower mantle, which was required by the data. The seismic structure of the two compositional cases, linked to different thermal profiles, are very similar. Only in proximity of mantle discontinuities, is it possible to observe some variations between the two. However, C2 leads to more realistic thermal structures. In the depth range of interest, between 250 and 800 km, we note that both models are a bit slower and denser than the STW105 seismic model above 410 km and have more structure in the transition zone, consistent with the phase transitions predicted by mineral physics.

4.1 Long-period and *SS* precursors waveforms

By using normal mode summation, we computed synthetic waveforms for our best-fitting models and compared them with seismic reference models and data. An example of long-period (>60 s) synthetic waveforms of the two best-fitting models for cases C1 and C2 compared with the STW105 and PREM synthetics is given

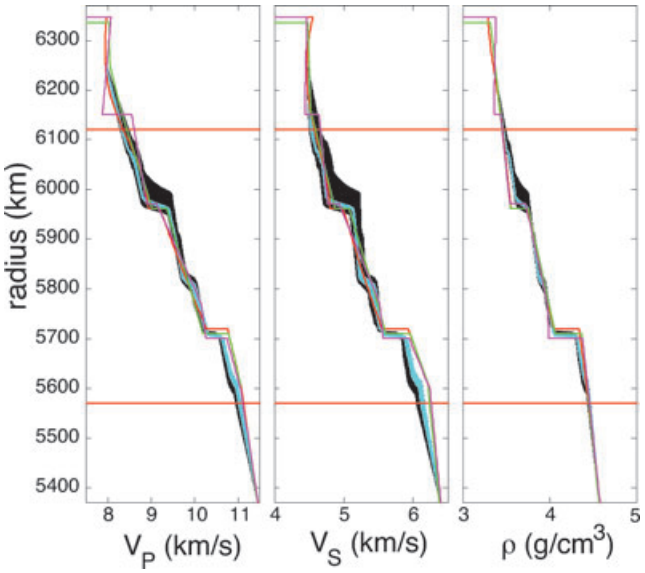

Figure 12. Seismic and density structure of the best-fitting models (in blue) for the case C1 (same figure for the case C2 is in Fig. S5). Red horizontal lines correspond to 250 and 800 km depth.

in Figs S6 and S7. As expected, the waveforms are very similar. PREM amplitudes of Love waves are slightly larger than the ones of STW105 and our best-fitting models. In general, we found that the largest discrepancy between the different 1-D models was, not surprisingly, at distances where fundamental and overtones arrive together. This is a result of the interference paths which enhances small differences between the 1-D models. Although this could seem promising for discrimination between the different models, interferences in real data are more complex, due to 3-D structure, and those wave packets are characterized by the lowest signal-to-noise ratio. We also compare the synthetics against the Berkeley collection of long-period waveforms (e.g. Panning & Romanowicz 2006). As expected, the variance reduction achieved by the physical models is very similar to the one obtained with seismic reference models. This result confirms the feasibility to use our physical models as starting models in 3-D inversions.

We also present an example of computed *SS* precursors waveforms, that are the underside reflections to mantle discontinuities which arrive earlier than the main *SS* phase. Each discontinuity is associated with a *SdS* phase, where *d* is the depth of the discontinuity. *SS* precursors phases are recorded on the transverse component and are best seen at a periods between 15 and 75 seconds and at an epicentral distance between 100° and 160°. *SdS* phases are sensitive to the impedance jump ($V_S \times \rho$) of the discontinuities. They are, therefore, a useful complementary data set to long-period data that are not sensitive to the jumps across discontinuities. The phases have a weak signal on single seismograms. A stacking procedure is necessary to enhance the signal-to-noise ratio of coherent arrivals (for a review, see Deuss 2009). Here, we only aim to illustrate the expected variations between the physical models, which fit global seismic data. We computed *SS* precursors waveforms for the best-fitting models for the cases C1 and C2 using normal mode summation down to a period of 10 s. Synthetics are bandpass filtered between 15 and 75 s. Tests at several epicentral distances have been performed. Here, we show an example at an epicentral distance of 100°.

In the top panel of Fig. 15, it is possible to note the strong similarity of the *S* and *SS* phases in the STW105 reference model compared to our two models. Note that the two models represented here are the best-fitting models after increasing the velocities at the top of lower mantle. The *SS* phase in the unperturbed models arrive almost 10 s later (see also Fig. 11 at $\Delta = 50°$: the arrival of *SS* doubles the delay of the main S phase recorded at half of the epicentral distance). The S410S of the C2 best-fitting model has slightly smaller amplitudes (Fig. 15, bottom panel) because of the smaller impedance jump due to the less olivine content in C2 compared to the C1 case. The differential traveltime S660S–S410S of the two models, which gives an estimate of the transition zone thickness, is very similar and, in both cases, longer by about 7 s than what is predicted with the STW105 model (Fig. 15, bottom panel). The similarity of the waveforms cast doubts on the possibility to discriminate between the two compositional cases based upon *SdS* measurements. This is consistent with the findings of Xu *et al.* (2008) that the width and velocity of the transition zone are largely insensitive to basalt fraction if a mechanical mixture of MORB and Harzburgite is considered. This property that has been exploited to infer robustly the temperature of this region from *SdS* differential traveltime measurements (Ritsema *et al.* 2009). On the other hand, both amplitude and phases predicted by the two best-fitting models appear compatible with reference seismic models. For comparison, we show the *SS* precursors waveform of the recent Harvard 1-D model, STW105. The variation between PREM and STW105 (shown in Fig. S8) is more pronounced than the variation between the C1 and C2 best-fitting models. This is due to the different depths of the transitions plus the 220 km discontinuity. For example, the differential traveltime S660S–S410S is 10 s less for PREM than for STW105.

Looking at the best-fitting models of Fig. 14, we note that the jump in V_S around 410 km is always higher than what it is in seismic models. On the other hand, the density jump is smaller and so the impedance jump is not much different than in seismic models. In our case, both density and seismic velocities are predicted by mineral physics. The density jump of seismic models is not constrained by data. Therefore, interpreting the velocity jumps based on *SS* (or PP) precursors in terms, for example, of olivine content, gives a wrong estimate if the assumed density jump is wrong. Note also that the finite depth that characterizes the discontinuities of the physical models (Fig. 14) also tend to reduce the amplitudes of the waveforms compared to sharp boundaries. For instance, the inflection in seismic structure around 520 km does not produce a visible anomaly at frequencies used for the *SS* precursors waveforms.

In order to compare our models against data, a careful reprocessing of *SS* data should be done. This is outside the scope of this paper. However, we note that in globally stacked *SS* precursors traces, the differential traveltime S660S–S410S is shorter than PREM (which actually has discontinuities at 400 and 670 km) and that the 220 km is not a global feature (e.g. Deuss 2009). The signal of a discontinuity at 520 km is also absent in globally stacked traces. All the features are substantially in good agreement with what is predicted by the physical models.

4.2 Attenuation

In previous tests, we showed the results obtained with an attenuation seismic structure, taken from the model QL6. We also performed tests by modelling the *P*, *T*, frequency and grain size dependence of *Q* with physical models based on mineral physics. Specifically, we used six *Q* models based on a homologous temperature approach from Cammarano *et al.* (2003) and the model of Faul & Jackson

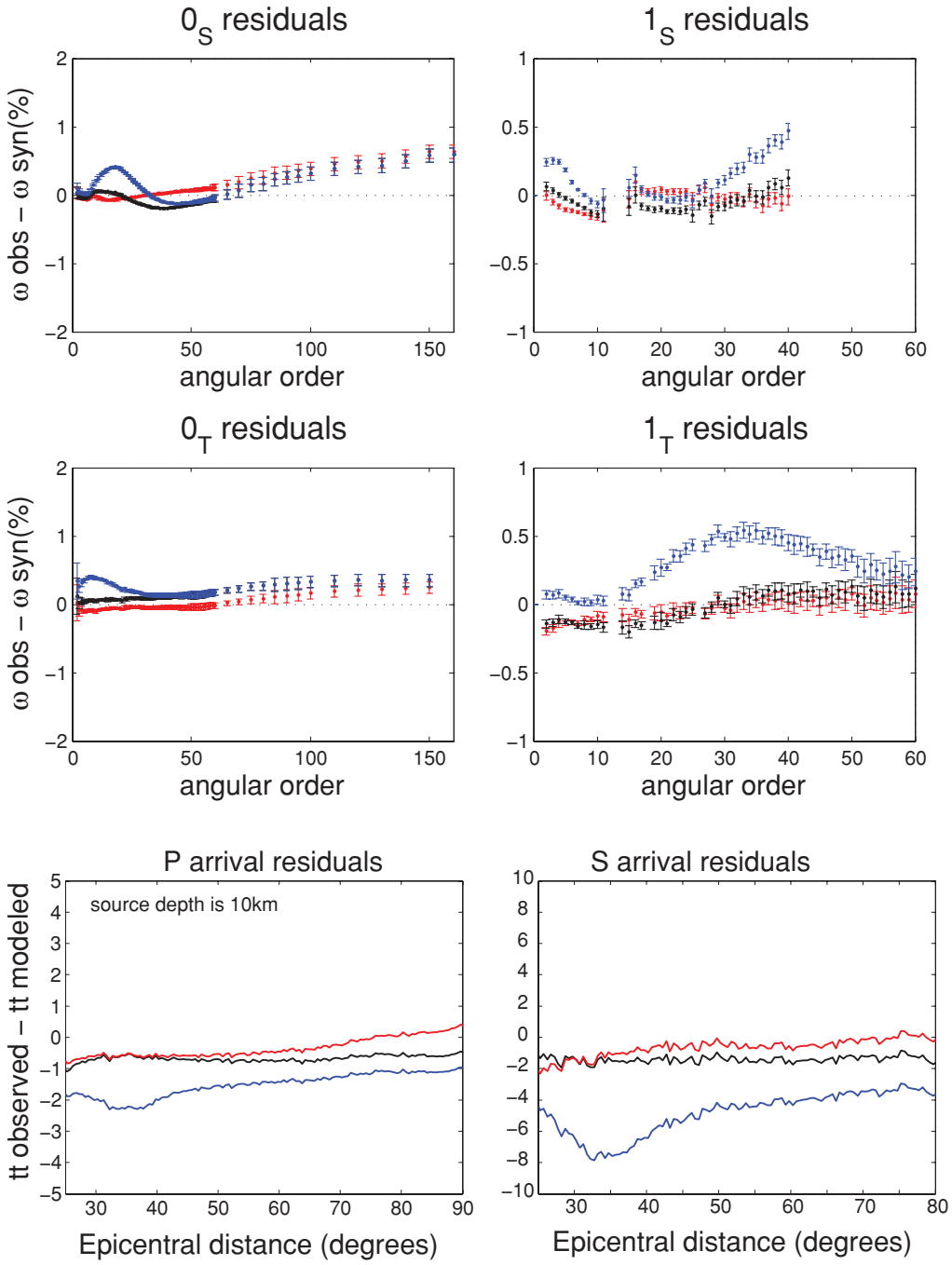

Figure 13. Residuals to spheroidal modes (top panels), toroidal modes (middle panels) and traveltimes (bottom panels) of the best-fitting model (in black), after the velocity correction for the case C1 (see text) compared to the same model before the correction (in blue). STW105 residuals are in red.

(2005), which is based on experiments on polycrystalline olivine. All the physical laws are assumed to be valid for bulk composition and to be insensitive to composition. Owing to the large uncertainties in Q laws, these tests are not done to improve the thermal interpretation, but to test whether the parameters that enter into the physical models are compatible with seismic data. Modelling the well-known T dependence of Q for 3-D studies, however, is recommended to improve interpretation.

We model the Q_S values assuming a reference period of 150 s to compare our results with the QL6 model, that is based on long-period data. All the anelasticity models considered require temperatures between 1450 and 1650 K to get the QL6 value at 150 km (Fig. 16). The Q5 model and the model of Faul & Jackson at a grain size of ∼1 cm take very similar values at this depth. The temperatures predicted by the Q models are overall consistent with the ones inferred from petrological considerations (Cammarano & Romanowicz 2008). Due to the uncertain P dependence, the outcome of the models diverges with depth (Fig. 16). As discussed in the introduction, the models by Cammarano *et al*. adopt a homologous T approach, while a constant value of activation volume is used in the Faul & Jackson's model. The temperatures of the best-fitting models at 450 km are around 1700 K for the case C1 and 1650 K for the case C2. The Q_S values predicted by the Cammarano's models agrees well with the seismic ones at this T (Fig. 16). This is not

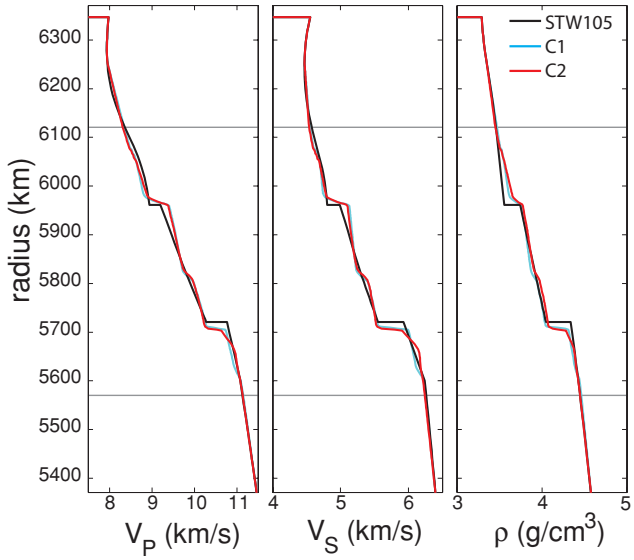

Figure 14. Seismic and density structure of the best-fitting models for case C1 and C2 compared to STW105 (see legend).

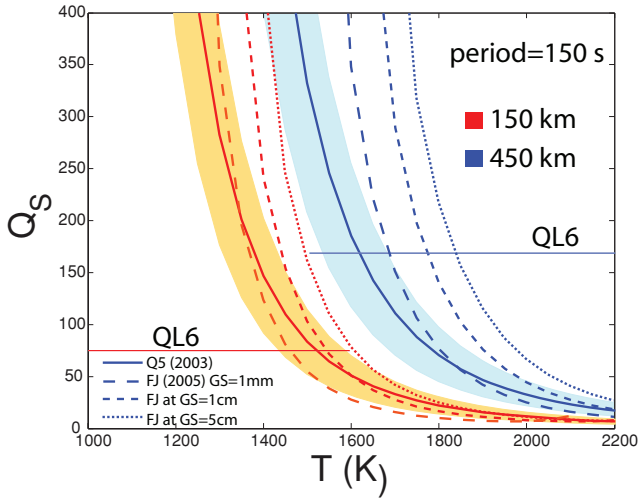

Figure 16. Temperature and pressure dependence of the Q physical models used in this study. Solid lines refer to the Q5 model of Cammarano *et al.* (2003). Shaded areas include all the values obtained with the other five models of Cammarano *et al.* (2003). Dashed lines refer to the Faul & Jackson's model (2005) at different grain size (see legend). In red, we plot the values at 150 km, in blue, the values computed at 450 km. QL6 values at these two depths are also plotted. All the quality factors are computed at a period of 150 s.

completely surprising, as the absolute values of the hybrid models of Cammarano *et al.* (2003) are tuned to be similar to seismic models along a mantle adiabat. Note, however, that the P dependence used is able to reproduce well the values expected from seismic studies at different depths. The Faul & Jackson model, on the other hand, attains the seismic Q_S values at higher temperatures than what is predicted by our inversion (Fig. 16). Of course, the Faul & Jackson's model is based on experiments on olivine at low pressure and it should not expected to be valid in the domain of wadsleyite.

With the thermal structures attached to our best-fitting models, we predict the Q profile for our best-fitting models (Fig. 17, panel a) and we compute their fit to measurements of seismic attenuation, following the procedure of Cammarano & Romanowicz (2008). In spite of the negative thermal gradient just below 250 km which characterizes the best-fitting model for the case C1, the effects on Q are not significant. Indeed, we found that the two best-fitting

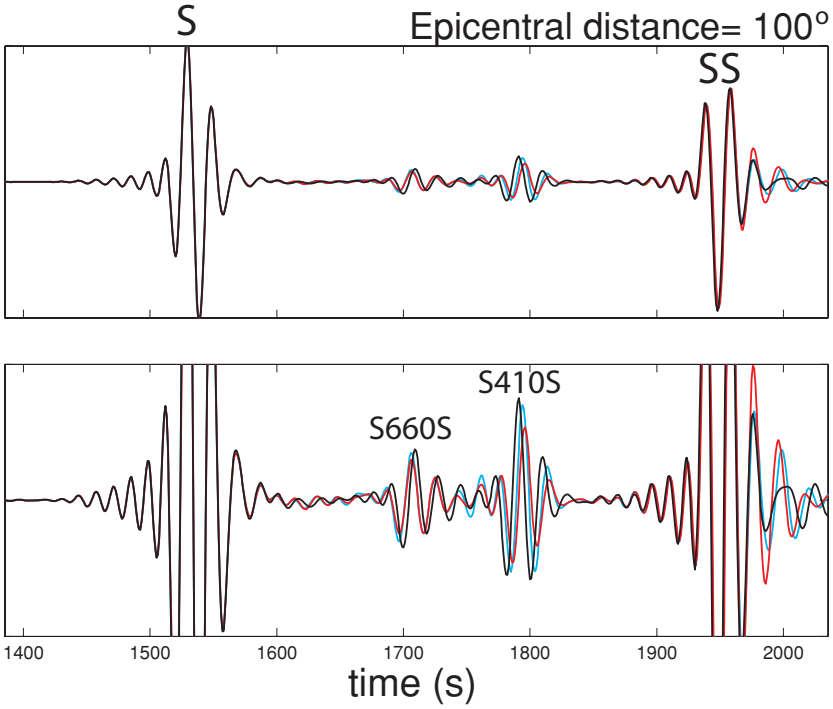

Figure 15. SS precursors waveforms for the best-fitting models, C1 in blue, C2 in red and the seismic reference model STW105, in black. PREM synthetics are given in Fig. S7. Seismograms are filtered between 15 and 75 s. Receiver is at epicentral distance of 100°. Bottom panel is amplified four times compared to the top one to highlight *SdS* phases.

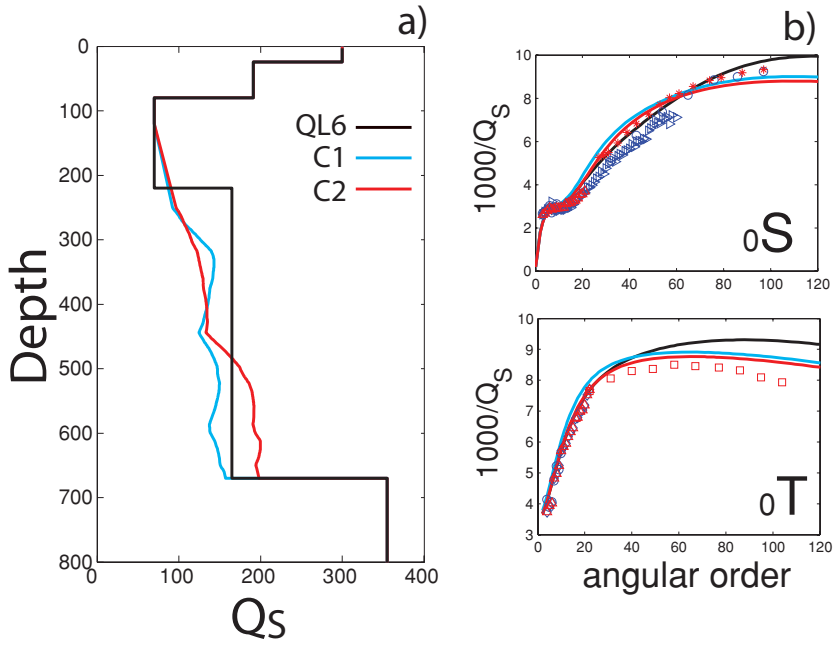

Figure 17. Shape of the two attenuation profiles for the best-fitting models of the case C1 (blue) and C2 (red), based on the Q5 model (panel a). Residual to fundamental spheroidal and toroidal observations of seismic attenuation are given in panel (b). Data include compilations of surface wave and free oscillations attenuation available on the REM webpage (e.g. Cammarano & Romanowicz 2008).

models for C1 and C2 cases fit the observations in a similar manner whatever Q model is used. When the model Q5 is used, the fit to the data is generally consistent with the QL6 model (Fig. 17, panel b). Nevertheless, if an equilibrium assemblage is assumed instead of a mechanical mixture, the thermal gradient required by the data is much stronger (as shown in Fig. 4) and results, in this case, in values of Q which are not reconcilable with seismic observations.

5 DISCUSSION

The analysis of normal mode and traveltimes with the reference mineral physics model indicate that either a negative thermal gradient or an enrichment in MORB with depth are required below 250 km. This result confirms our previous findings based on long-period seismic waveforms (Cammarano & Romanowicz 2007). As discussed previously, we tend to favour the compositional explanation, because this is consistent with geodynamic models and can also explain some geochemical features. Alternatively, an increase in grain size from mm scale to several centimetres has been proposed to explain the V_S gradient inferred from seismic data (Faul & Jackson 2005). In general, an increase in grain size is compatible with a transition from dislocation creep regime in the shallow upper mantle, usually accompanied by recrystallization, to a diffusive deformation mechanism deeper. The grains should not be able to grow indefinitely, however, because of the poliphase and polycrytalline nature of mantle rocks (Olgaard & Evans 1988). It is not clear if such a large increase with depth is dynamically possible and if it is really happening within the Earth. This possibility should not be excluded, but we must keep in mind that the growing evidence of heterogeneity in the upper mantle seems to indicate an environment unfavourable for grain growth. In addition, it must be pointed out that the role of grain size at upper-mantle conditions is still unclear. Conversely to a thermal and/or compositional interpretation, a purely grain size interpretation does not affect much the V_P structure of the upper mantle and does not affect at all density and the phase transitions of the upper mantle. Seismic attenuation in the mantle is likely to be dependent on grain size, as found in the experiments modelled by Faul & Jackson. Similarly to a decrease in temperature with depth, increasing grain size will reduce attenuation. Measurements of seismic attenuation, however, can be explained by using the Faul & Jackson model with simple thermal and grain size structures and there is no need to vary grain size with depth (Cammarano & Romanowicz 2008). In any case, we cannot exclude a purely grain size explanation based uniquely on attenuation data as uncertainties in the physical law of Q are large.

By using our procedure, we can test if our best-fitting T–C models fit additional data that are sensitive to mantle discontinuities or to P-velocity structure. For example, *SS* precursor waveform add useful information on the impedance jumps at the mantle discontinuities. As discussed in the previous section, it would probably be hard, however, to separate compositional, thermal or grain size effects based uniquely on these data. Coupling *SS* and *PP* precursors could probably help.

Assuming an isothermal structure, we estimated that a doubling of MORB component in less than 100 km would be necessary in order to fit the seismic data. This result is not dependent on the specific mineral physics model used, being mostly based on the well-constrained pressure derivatives of the elastic properties of mantle minerals. Indeed, other models (e.g. Cammarano *et al.* 2003) have very similar velocity gradients for the same T structure. It is very difficult to produce such a large compositional gradient dynamically. Therefore, it is reasonable to expect that an increase in grain size could, nevertheless, have some role.

In general, the proposed procedure will benefit from future advances in understanding material properties at high pressure and temperature. At the same time, as shown in this paper, the interpretation of geophysical observations will guide the mineral physics research to focus on key parameters and it provides a robust test of the model used. For example, we find that the elastic properties

of the lower mantle obtained with the XSLB08 model are not able to match simultaneously traveltime and normal mode data. The increase in velocity at the top of the lower mantle required by the seismic data falls within the uncertainty in the mineral physics data, highlighting the need for better experimental constraints. Smaller, but still significant uncertainties on the elastic properties of the transition zone minerals hamper a precise estimation of the absolute temperature of the upper mantle. Using our mineral physics model, we found a ∼200 K colder mantle than what is predicted from a mantle adiabat (see Fig. 8). Elasticity values of a few percent higher for the mantle transition zone minerals would compensate such a difference in temperature.

6 CONCLUSIONS

We presented a procedure to test a mineralogical model of the upper mantle against seismic observations. The model is based on current knowledge of material properties at high temperatures and pressures. We focus on average structure between 250 and 800 km.

Normal mode and traveltime data impose robust constraints on the thermochemical structure of the upper mantle. We obtained a series of important results which are robust and do not depend on the specific mineral physics model used. Specifically, we found that it is not possible to explain the data with any equilibrium composition. A mixture of MORB and harzburgite, with the MORB component increasing with depth, is able to reproduce well all the seismic data for realistic thermal structures. If the proportions of MORB with depth do not change, negative thermal gradients below 250 km are necessary to explain the data. We note that such negative thermal gradients are not compatible with recent geodynamic models, which instead see a compositional gradient with depth. Based on the mineral physics model tested, we estimate almost a doubling in MORB component within less than 100 km for an isotherm. Such an enrichment in basalt component is probably not dynamically feasible. An increase in grain size could help to reduce the required compositional gradient below 250 km. Residual uncertainties in pressure derivatives of mantle minerals could also slightly affect interpretation.

Velocities predicted by the reference mineral physics model at the top of the lower mantle are too low. This result highlights the importance of performing, for the first time, *in situ* experimental measurements of the elastic properties of lower mantle phases at the pressure–temperature conditions of the lower mantle. A harzburgite layer at the top of the lower mantle can be formed dynamically within a not-equilibrated mantle. Harzburgite is faster than pyrolite. Therefore, the presence of such a layer would be more compatible with seismic data, although it would not be sufficient. If the properties of the lower mantle turn out to be correct, an unrealistic negative thermal gradient between upper and lower mantle would be required. Owing to the uncertainties in the mineral physics model, caution should be used also regarding the absolute values of temperature of the upper mantle, that appear to be ∼200 K colder than adiabatic values. Though velocity gradients with depth are well constrained from mineral physics for a given thermal profile, uncertainties in absolute values are still large and hamper a precise interpretation in terms of absolute temperatures. The thermal structures obtained, however, can be translated into attenuation profiles that are consistent with measurements of seismic attenuation. Note that this is not the case for an equilibrium assemblage, which would require too low temperatures (and attenuation) around 300 km.

The long-period seismograms of the best-fitting thermal models with either average pyrolitic composition or a compositional profile derived from geodynamic modelling (both assuming a mixture of MORB and harzburgite components) are very similar. The models fit the long-period waveforms well enough to be used as starting models in 3-D inversions. Some differences in the seismic response of the alternative *T*–*C* structures emerge at higher frequencies. In particular, variations near mantle phase transitions can produce small, but systematic variations in *SS* precursors waveforms. For example, amplitudes of the S410S phase decrease when the MORB component around this depth increases.

Extending our procedure to other seismic and density data and interpreting the 3-D structure is promising to get a better insight on the thermochemical structure of the upper mantle. For example, a study on regional variations of *SS* precursors waveforms combined with long-period data may improve constraints on the upper-mantle physical (i.e. *T* and *C*) structure. In addition, the same database of material properties can be used in dynamic models to test whether the thermochemical structure inferred from geophysical observations is consistent with Earth's evolution.

ACKNOWLEDGMENTS

We thank Ian Jackson and an anonymous reviewer for comments that improved the paper. This work is partially supported by the European Commission under the Marie Curie Intra-European Fellowship Programme (no. 219870).

REFERENCES

Aizawa, Y., Barnhoorn, A., Faul, U., Gerald, J.F. & Jackson, I., 2008. The influence of water on seismic wave attenuation in dunite: an exploratory study, *J. Petrol.,* **49,** 841–855.

Anderson, D., 2006. Speculations on the nature and cause of mantle heterogeneity, *Tectonophysics,* **416,** 7–22.

Buland, R. & Chapman, C.H., 1983. The computation of seismic travel times, *Bull. seism. Soc. Am.,* **73,** 1271–1302.

Cammarano, F. & Romanowicz, B., 2007. Insights into the nature of the transition zone from physically constrained inversion of long-period seismic data, *PNAS,* **104,** 9139–9144.

Cammarano, F. & Romanowicz, B., 2008. Radial profiles of seismic attenuation in the upper mantle based on physical models, *Geophys. J. Int.,* **175,** 116–134.

Cammarano, F., Goes, S., Vacher, P. & Giardini, D., 2003. Inferring upper mantle temperatures from seismic velocities, *Phys. Earth planet. Inter.,* **139,** 197–222.

Cammarano, F., Deuss, A., Goes, S. & Giardini, D., 2005a. One-dimensional physical reference models for the upper mantle and transition zone: combining seismic and mineral physics constraints, *J. geophys. Res.,* **110,** B01306, doi:10.1029/2004JB003272.

Cammarano, F., Goes, S., Deuss, A. & Giardini, D., 2005b. Is a pyrolitic adiabatic mantle compatible with seismic data? *Earth planet. Sci. Lett,* **232,** 227–243.

Chambers, K., Deuss, A. & Woodhouse, J., 2005. Reflectivity of the 410-km discontinuity from PP and SS precursors, *J. geophys. Res.,* **110,** doi:10.1029/2004JB003345.

Cobden, L., Goes, S. & Cammarano, F., 2008. Thermo-chemical interpretation of one-dimensional seismic reference models for the upper mantle: evidence for bias due to heterogeneity, *Geophys. J. Int.,* **175,** 627–648.

Cobden, L., Goes, S., Ravenna, M., Styles, E., Cammarano, F. & Connolly, J., 2009. Thermochemical interpretation of 1-d seismic data for the lower mantle: the significance of non-adiabatic thermal gradients and compositional heterogeneity, *Geophys. J. Int.,* in press.

Crotwell, H., Owens, T. & Ritsema, J., 1999. The taup toolkit: flexible travel time and ray path utilities., *Seismol. Res. Lett.,* **70,** 154–160.

Dahlen, F. & Tromp, J., 1998. *Theoretical Global Seismology,* Princeton University Press, Princeton, NJ.

Dalton, C., Ekström, G. & Dziewonski, A., 2009. Seismological and experimental observations of shear velocity and attenuation: a global comparison, *Earth planet. Sci. Lett,* **284,** 65–75.
Deuss, A., 2009. Global observations of mantle discontinuities using SS and PP precursors, *Surv. Geophys.,* in press, doi:10.1007/s10712-009-9078-y.
Durek, J. & Ekström, G., 1996. A radial model of anelasticity consistent with long period surface-wave attenuation, *Bull. seism. Soc. Am.,* **86,** 144–158.
Dziewonski, A. & Anderson, D., 1981. Preliminary reference earth model, *Phys. Earth planet. Inter.,* **25,** 297–356.
Engdahl, E., der Hilst, R.V. & Buland, R., 1998. Global teleseismic earthquake relocation with improved travel times and procedures for depth determination., *Bull. seism. Soc. Am.,* **88,** 3295–3314.
Faul, U. & Jackson, I., 2005. The seismological signature of temperature and grain size variations in the upper mantle, *Earth planet. Sci. Lett.,* **234,** 119–134.
Gaherty, J. & Jordan, T., 1995. Lehmann discontinuity as the base of an anisotropic layer beneath continents, *Science,* **268,** 1468–1471.
Gung, Y., Panning, M. & Romanowicz, B., 2003. Global anisotropy and the thickness of continents, *Nature,* **422,** 707–711.
Hill, R., 1952. The elastic behaviour of a crystalline aggregate, *Proc. Phys. Soc. Lond. Sect.,* **65,** 349–355.
Hirschmann, M., 2000. Mantle solidus: experimental constraints and the effects of peridotite composition, *Geochem. Geophys. Geosyst.,* **1,** paper 2000GC000070.
Irifune, T. & Ringwood, A., 1993. Phase-transformations in subducted oceanic-crust and buoyancy, *Earth planet. Sci. Lett,* **117,** 101–110.
Irifune, T., Higo, Y., Inoue, T., Kono, Y. Ohfuji, H. & Funakoshi K., 2008. Sound velocities of majorite garnet and the composition of the mantle transition region, *Nature,* **451,** 814–817.
Jackson, I., 2008. Properties of rocks and minerals—physical origins of anelasticity and attenuation in rock, in *Treatise on Geophysics,* Vol. 2, pp. 493–525, Elsevier, Amsterdam.
Karato, S., 1993. Importance of anelasticity in the interpretation of seismic tomography, *Geophys. Res. Lett.,* **20,** 1623–1626.
Kennett, B., Engdahl, E. & Buland, R., 1995. Constraints on seismic velocities in the earth from travel times, *Geophys. J. Int.,* **122,** 108–124.
Kustowski, B., Ekström, G. & Dziewonski, A., 2008. Anisotropic shear-wave velocity structure of the Earth's mantle: a global model, *J. geophys. Res,* **113**(B6), B06306, doi:10.1029/2007JB005169.
Matas, J., Bass, J., Ricard, Y., Mattern, E. & Bukowinski, M., 2007. On the bulk composition of the lower mantle: predictions and limitations from generalized inversion of radial seismic profiles, *Geophys. J. Int.,* **170**(2), 764–780.
Olgaard, D. & Evans, B., 1988. Grain-growth in synthetic marbles with added mica and water, *Contrib. Mineral. Petrol.,* **100**(2), 246–260.
Panning, M. & Romanowicz, B., 2006. A three dimensional radially anisotropic model of shear velocity in the whole mantle, *Geophys. J. Int.,* **167,** 361–379.
Ritsema, J., Xu, W., Stixrude, L. & Lithgow-Bertelloni, C., 2009. Estimates of the transition zone temperature in a mechanically mixed upper mantle, *Earth Planet. Sci. Lett.,* **227,** 244–252.
Romanowicz, B. & Mitchell, B., 2007. Q in the earth from crust to core, in *Treatise on Geophysics,* Vol. I, pp. 731–774, Elsevier, Amsterdam.
Schmerr, N. & Garnero, E., 2007. Upper mantle discontinuity topography from thermal and chemical heterogeneity, *Science,* **318**(5850), 623–626.
Shearer, P., 2000. Upper mantle seismic discontinuities, in *Earth's Deep Interior: Mineral Physics and Tomography from the Atomic to the Global Scale.,* Geophysical Monograph 117, pp. 115–131, AGU.
Stixrude, L. & Lithgow-Bertelloni, C., 2005a. Thermodynamics of mantle minerals—I. Physical properties, *Geophys. J. Int.,* **162**(2), 610–632.
Stixrude, L. & Lithgow-Bertelloni, C., 2005b. Mineralogy and elasticity of the oceanic upper mantle: origin of the low velocity zone, *J. geophys. Res.,* **110,** B03204, doi:10.1029/2004JB002965.
Tackley, P., Xie, S., Nakagawa, T. & Hernlund, J., 2005. Numerical and laboratory studies of mantle convection: philosophy, accomplishments, and thermochernical structure and evolution, in *Earth's Deep Mantle: Structure, Composition, and Evolution,* Vol. 160, pp. 83–99, Geophysical Monograph, AGU.
Thybo, H., Nielsen, L. & Perchuc, E., 2003. Seismic scattering at the top of the mantle transition zone, *Earth planet. Sci. Lett,* **216**(3), 259–269.
Weertman, J., 1970. The creep strength of the earth's mantle, *Rev. Geophys.,* **8,** 145–168.
Williams, Q. & Revenaugh, J., 2005. Ancient subduction, mantle eclogite, and the 300 km seismic discontinuity, *Geology,* **33,** 1–4.
Woodhouse, J., 1988. The calculation of eigenfrequencies and eigenfunctions of the free oscillations of the earth and the sun, in *Seismological Algorithms,* pp. 321–370.
Xu, W., Lithgow-Bertelloni, C., Stixrude, L. & Ritsema, J., 2008. The effect of bulk composition and temperature on mantle seismic structure, *Earth planet. Sci. Lett.,* **275,** 70–79.

SUPPORTING INFORMATION

Additional Supporting Information may be found in the online version of this article:

Figure S1. Effects on velocity gradients starting from a different reference composition (top panel) or temperature (bottom panel) at 250 km depth. Solid lines refer to the standard case reported also in Fig. 4, with $C(250\ \text{km}) = 0.17$ and $T = 1700$ K. In the top panel, dashed lines are for $C = 0$ (i.e. harzburgite), dot–dashed lines with $C = 0.34$. In the bottom panel, dashed lines are with $T(250\ \text{km}) = 1850$ and dot–dashed lines with $T(250\ \text{km}) = 1550$ K. Different colours refer to three thermal structures (see legend).
Figure S2. Residual eigenfrequencies for spheroidal modes of the best-fitting models for case C2 (in black). The trend of seismic models is also plotted (see legend). Seismic models use the same colour scheme of Fig. 9. Mean frequencies data are from REM webpage. Bounds of residual values refer to the standard deviations of frequency data.
Figure S3. Residual eigenfrequencies for toroidal modes of the best-fitting models, case C2 (in black). Seismic models use the same colour scheme of Fig. 9. Mean frequencies data are from REM webpage. Bounds of residual values refer to the standard deviations of frequency data.
Figure S4. Traveltime residuals for *P* and *S* phases to the EHB data (Engdahl *et al.* 1998) for case C2. In black, best-fitting models for traveltimes, in green best-fitting models for modes. Other lines refer to seismic reference model, same colour scheme as in Fig. 9.
Figure S5. Seismic and density structure of the best-fitting models (in blue) for the case C2. Red horizontal lines correspond to 250 and 800 km depth.
Figures S6 and S7. Example of a transverse component, long-period seismogram (bandpass filtered from 60 to 250 s) for an hypothetical right-lateral strike slip fault at 10 km depth. Receiver is in line with the fault motion and at epicentral distance of 60°. Synthetics for the best-fitting model of the case C1 and C2 are, respectively, in light blue and red. STW105 synthetics are in black. PREM synthetics are shown in Fig. S7 in green. Second panel from the top highlights the arrivals of SH body waves followed by the minor arc Love wave. Close up of minor arc (L1) and major arc (L2) Love waves are given in the two panels at the bottom.
Figure S8. *SS* precursors waveforms for PREM (in green) and STW105 (in black). Seismograms are filtered between 15 and 75 s. Receiver is at epicentral distance of 100°. Bottom panel is amplified four times compared to the top one to highlight *SdS* phases.

Please note: Wiley-Blackwell are not responsible for the content or functionality of any supporting materials supplied by the authors. Any queries (other than missing material) should be directed to the corresponding author for the article.